SKB TECHNICAL REPORT

88-29

Modelling of buffer material bahaviour. Some examples of material models and performance calculations

Lennart Börgesson

Clay Technolology AB, Lund, Sweden

December 1988

MODELLING OF BUFFER MATERIAL BEHAVIOUR

SOME EXAMPLES OF MATERIAL MODELS AND PERFORMANCE
CALCULATIONS

Lennart Börgesson

Clay Technology AB, Lund, Sweden

December 1988

MODELLING OF BUFFER MATERIAL BEHAVIOUR.

SOME EXAMPLES OF MATERIAL MODELS AND PERFORMANCE CALCULATIONS.

Lennart Börgesson

Clay Technology AB
Lund, Sweden

CONTENTS   *page*

SUMMARY

Some material models of smectite rich buffer material suited for nuclear
waste isolation are accounted for in the report. The application of
these models in finite element calculations of some scenarios and
performances are also shown.

The rock shear scenario has been closely studied with comparisons
between calculated and measured results. Sensitivity analyses of the
effect of changing the density of the clay and the rate of shear have
been performed as well as one calculation using a hollow steel cylinder.

Material models and finite element calculations of canister settlement,
thermomechanical effects and swelling are also accounted for.

The report shows the present state of the work to establish material
models and calculation tools which can be used at the final design of
the repository.

PREFACE

SYMBOLS

c_v	coefficient of consolidation at constant pressure
c_p	coefficient of consolidation at constant volume
F_m	displacement magnification factor
P	average stress
t	time
t_r	reference time
T_f	shear strength
V	degree of consolidation
δ	displacement
ε	strain
ε_p	plastic strain
$\dot{\gamma}$	rate of strain
$\dot{\gamma}_o$	reference rate of strain
ρ	density
ρ_m	density at saturation
σ_j	Mises stress
$(\sigma_1 - \sigma_3)$	deviator stress
$(\sigma_1 - \sigma_3)_f$	deviator stress at failure

1. INTRODUCTION

All Swedish concepts regarding nuclear waste disposal involve clay barriers as near field isolation or tunnel, shaft and borehole plugging. The final geometry and clay material are yet to be decided and as a basis for these desicions different performance calculations must be made. These calculations involve both the "normal" performance of the near field during the repository life-time and the "unnormal" possible scenarios.

The main Swedish concept (KBS 3) is shown in Fig. 1:1. The waste will be enclosed in copper canisters surrounded by an annulus of highly compacted Na-bentonite with a thickness of 37 cm. The canister will be placed in 7.5 m deep holes having a diameter of 1.5 m which are drilled from the base of long tunnels in crystalline rock at a depth of at least 500 m. The performance calculations are made assuming this geometry, but the models are made more general in order to allow for other geometries.

Calculation of the normal performance should include the following simulations:

* Canister settlement
* Temperature development
* Thermomechanical effects
* Buffer swelling and consolidation (eg homogenization)
* Unsaturated and saturated flow
* Diffusion
* Sealing effects

The "unnormal" performance should include:

* Quick undrained rock displacements
* Slow drained rock displacements
* Material degradation
* Canister failure

This report will deal with some of the normal performances (canister settlement, thermomechanical effects and buffer swelling and

7

BENTONITE/QUARTZ
WEIGHT
RELATIONSHIP
1:10 TO 1:5

CANISTER

HIGHLY COMPACTED
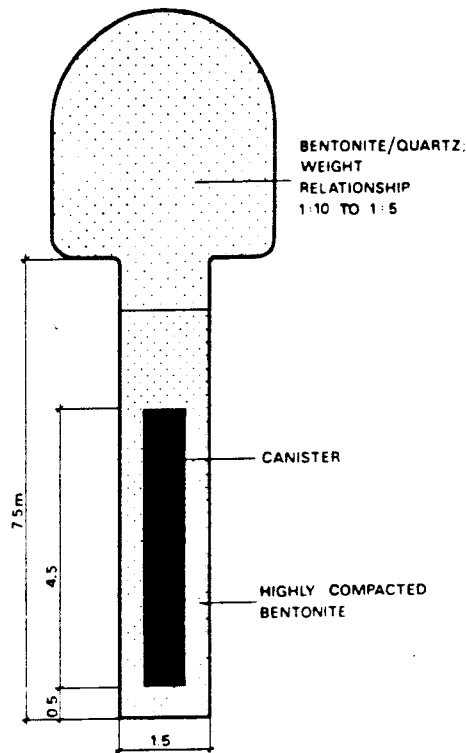BENTONITE

7.5 m

4.5

0.5

1.5

Fig 1:1 The Swedish main concept for high level radioactive waste
disposal

consolidation). It will also treat one "unnormal" performance (quick
rock shear).

It is of vital importance that the calculations are not only preceded by
careful laboratory tests in order to formulate material models, but also
accompanied by large scale laboratory tests or field tests in order to
evaluate and check the calculations. These calculations are often very
complicated. The simulation can be a 3-dimensional scenario which involves
many different materials with non-linear stress-strain behaviour and the
risk of drawing incorrect conclusions is great.

The purpose of modelling the buffer behaviour is to make performance
analyses and sensitivity analyses. Included in a total near field or
safety analysis, such calculations will be the basis of the final
repository design. An example of such a sensitivity analysis will be
shown in Chapter 4 (rock shear scenario).

2. CALCULATION TOOLS

The finite element method (FEM) has been chosen for doing most of the simulations. The reason for that choice is that FEM is a widely used technique, and there are many very qualified and well tested codes.

For simple purposes when the material model is simple and uncoupled (like temperature, diffusion and water flow), and the geometries are 2-dimensional codes like ENERGY, FEMTEMP, GEOFEM-C AND GEOFEM-G from the CHALMFEM system at Chalmers Technical University have been used. These codes have the advantage of being adapted to "engineering level" and easy to use. On the other hand they are very limited in usefulness.

For more qualified performance calculations there are several existing FE codes which could be used, e.g. ADINA, NASTRAN, ANSYS and ABAQUS. For the calculations referred to in this report has mainly ABAQUS been used. ABAQUS is specially designed for non-linear stress analyses.

In the existing ABAQUS code there is a large element library as well as a material model library for modelling different element types and different constitutive relations. The material models can often be combined in such a manner that no changes are required, but some models have been rewritten so as to adjuste the material model to the laboratory measured behaviour.

Usage of non-linear finite element codes is a very qualified task, especially for 3-dimensional models. There are often several different ways of making the calculation. Some of these ways may be equally good, but some may not lead to a correct solution and others may not lead to any solution at all (no convergence). It is thus important to be guided by experienced and highly qualified persons.

ABAQUS is in Scandinavia handled by FEMTECH AB. The calculations referred to in this report are being carried out at their office by the author and Jan Hernelind in cooperation.

3. ASPECTS OF PERFORMANCE ANALYSES

If a special scenario or a normal function is going to be analyzed one problem is to idealize the situation as much as possible without changing the results. All factors which have insignificant influence on the solution must be peeled off. If the influence of a factor is difficult to judge, a special analysis, possibly connected to a sensitivity study, must be carried out.

When making a scenario calculation it is also very important to choose the correct scenario and the choice must be dependent on the purpose of the calculation. If e.g. the effect of a rock movement is going to be simulated, the problem of how to localize the shear plane will arise. It can be shown that the canister is most affected if the shear plane goes horizontally through the center of the canister. If the purpose of the calculation is to design a repository and to choose the composition of the buffer material embedding the canister so that no damage to the canister can occur by any possible rock movement, then of course the worst possible scenario (horizontal central shear) must be studied. If, on the other hand, the purpose is to investigate the effect of a possible movement of the rock along a fracture pattern with a predominant angle of dip, another scenario has to be studied.

There are several steps connected to a performance calculation. In the first place a correct and well working material model has to be chosen or made. The non-linear complex behaviour of the buffer materials often makes it necessary to perform simulations of simple laboratory tests in order to check the models. When a well-working model is established, the next step is to make an element model of the structure, using suitable element types. If the structure is very complex, it might be wise to do a simplified model, e.g. in two dimensions, and to make test calculations on that model in order to study if the calculation leads to convergence in reasonable time and if it seems to yield reasonable results. At this stage it might be necessary to rearrange the structure or change the material model.

When satisfying results are reached, the real element model can be made and test calculations with a only a few iterations will be conducted. If

the model acts as expected, the calculation can be continued until the end. Very often it is, however, necessary to make adjustments in the element structure or to change element types before satisfactory results are reached.

Finally a sensitivity study can be made in order to fulfill the work. This can usually be conducted with little man power if the changes in structure or material parameters are small. Major changes may require new trials from step 2.

4. ROCK DISPLACEMENTS

4.1 General

The effect of a rock displacement across a deposition hole is a type of
"unnormal" scenario that must be taken into consideration. As was
mentioned in Chapter 3, the most dangerous case is the case of a
horizontal shear across the centre of the canister. The scenario is
shown in Fig 4:1.

The rock shear has been investigated by three large scale laboratory
tests. These tests are reported by Börgesson (1986). A summary of the
tests and a condensed validation of the FE calculations by comparison
will be presented in this chapter, as well as some sensitivity studies.

4.2 Large scale tests

Fig 4:2 and 4:3 show a photo and a drawing of the set-up. The length of
the simulated deposition hole was 60 cm and the diameter 16 cm, while
the copper canister had a length of 45 cm and a diameter of 8 cm. The
inside of the deposition hole was covered by sintered filters in order
to saturate the bentonite. The very stiff filter and steel tubes
simulating the rock were split in two halves to make the shearing
possible. One half was fixed in a very stiff frame, while the other one
was movable.

The required force was measured by three force transducers at the top of
the movable part. The effect of the shear on the canister was measured
by 5 strain gauges fixed to the canister. The normal pressure on the
canister and on the simulated rock surface was measured by 6 pressure
transducers. The force, the strain and the pressure were measured without
interruptions during the tests. Three tests with different rates of
deformation were performed.

4.3 Element model

The final 3-dimensional non-linear elastic-plastic calculations were
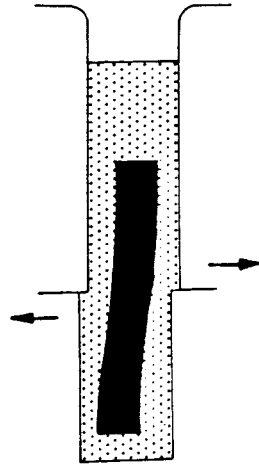preceeded by 2-dimensional linear elastic and non-linear elastic-plastic

Fig 4:1 The rock shear scenario

calculations in order to develope the technique and to check the convergence. Different element models were tested, and the model that yielded the best results was converted to three dimensions. A simplified 3D model was also preceeding the final calculations in order to check the boundary conditions, for example.

The 3D element model was simplified by using only one quarter of the total model. This was achieved cutting the model in the vertical symmetry plane in the shearing direction and in the horizontal anti-symmetry shear plane. The final model had a total number of 270 solid 3D elements consisting of 20 nodes, and 8 solid 3D elements consisting of 15 nodes. A view from above the model is shown in Fig 4:4 in which the canister is being marked with thick lines. The anti-symmetry shear plane corresponds to the bottom plane.

The boundary conditions are complex and extensive, with most of the nodes locked in at least one direction. Especially the anti-symmetri
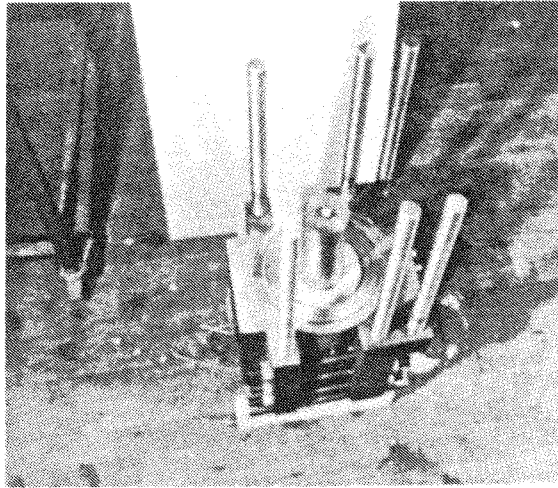
Fig 4:2 Mounting of the large scale test device. The lower fixed
cylinder and stiff frame are mounted as well as the copper
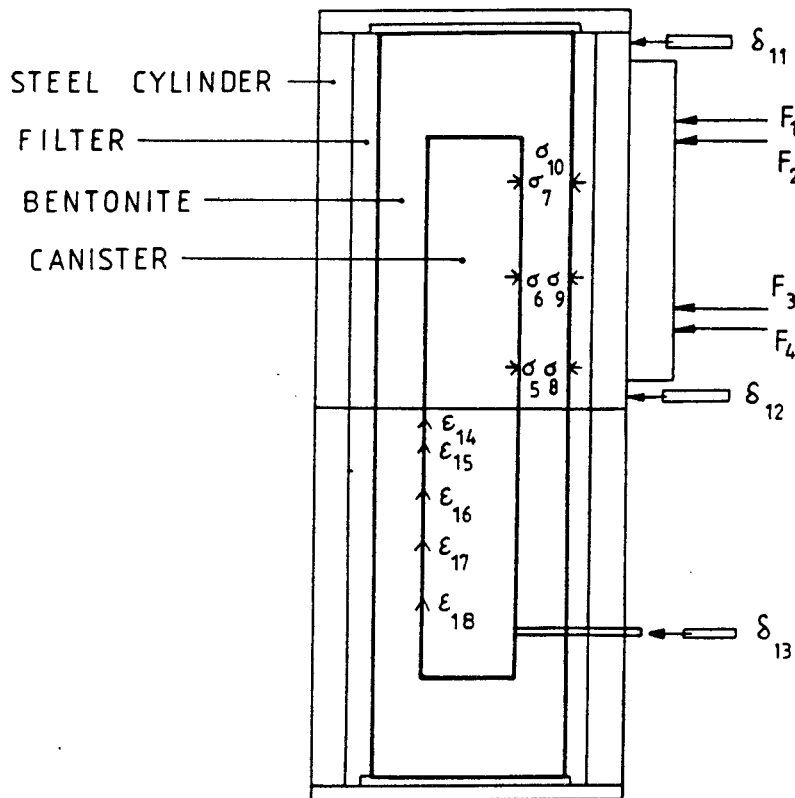canister and half of the compacted bentonite

Fig 4:3 Location of the transducers and guages in the large scale model

F_1-F_4 Force transducers

σ_5-σ_{10} Pressure transducers

δ_{11}-δ_{13} Strain transducers

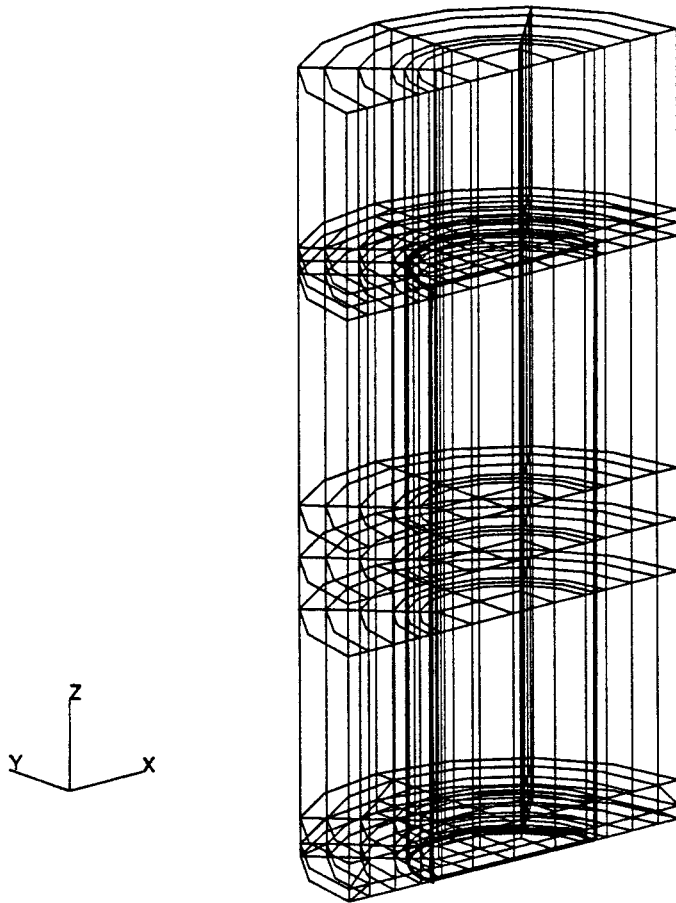ε_{14}-ε_{18} Strain guages

Fig 4:4 Element model at the rock shear simulation. The bottom plane
corresponds to the shear plane

shear plane creates problems and it is simulated by a 5 mm thick element
layer. The bottom nodes are fixed in the shear direction and free to
move upwards and downwards in the axial direction. By such a boundary
condition the prescribed rock displacement in the model will correspond
to half the real displacement. Since Poisson's ratio ν is 0.5 there will
be no volume change of the clay, although the boundary is free in the
axial direction.

4.4 Material model

In practice, the canister will consist of the spent fuel waste enclosed in
copper, but solid copper has been assumed in the calculations and in the
model. If the rock mass is considered to be infinitely rigid, only the two
materials clay and copper have to be modelled.

The clay is emplaced in a non-saturated state, but the process of
saturation is very fast, seen in the perspective of a repository

15

lifetime. This means that the saturated state is of primary interest. The properties of saturated smectite-rich clays have been investigated in various laboratory tests. In the large scale model tests Na-bentonite has been used. The properties of Na-bentonite are accounted for by Börgesson et al. (1988).

The basis of the material model is that it can be described by one simple non-linear stress-strain relation. This is possible under the following presumptions:

1. Undrained saturated conditions
2. Small differences in strain rates at different element locations
3. A change in external total pressure does not affect the stress-strain relation (no stress path dependence)

The shear must take place at such a fast rate, that presumption 1 is fulfilled. The material properties are rate-dependent, which means that presumption 2 must be fulfilled and the actual shear rate must be considered. The rate-dependence of the shear strength τ_f can be modelled as a function of the rate of strain $\dot{\gamma}$ according to Eqn 1:

$$\tau_f = m \left[\frac{\dot{\gamma}}{\dot{\gamma}_0} \right]^n \tag{1}$$

where m is the shear strength at $\dot{\gamma} = \dot{\gamma}_0$ and n is the factor expressing the rate-dependence. For smectite-rich clays $n = 0.05-0.1$.

The stress-strain relation of the clay thus varies with the rate of strain. In Fig 4:5 this relation is shown at different strain rates corresponding to the different strain rates in the large-scale model tests. The density at saturation is $\rho_m = 2.06$ t/m^3. The stress-strain relation shown in Fig 4:5 is typical for this clay with an initial linear elastic deformation until 1 % strain. After that the clay starts to yield non-linearily under strain-hardening and reaches a maximum shear stress at about 5% strain. The postfailure behaviour is not quite clear, but a constant shear resistant without peak is used in the material model.
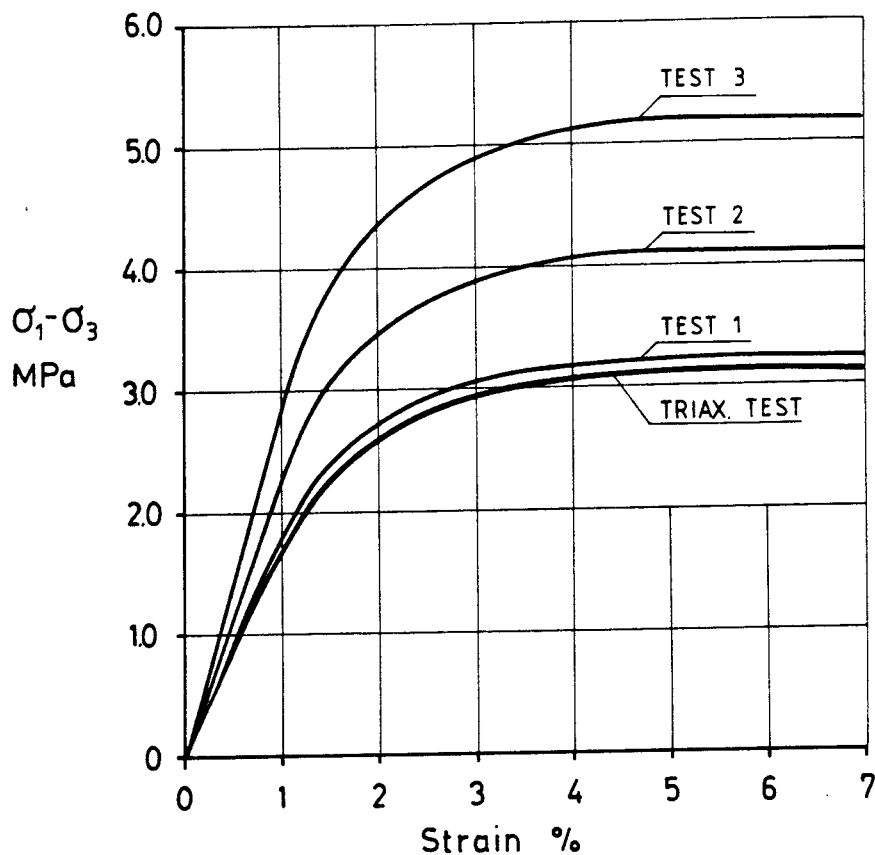
16

Fig 4:5 Stress-strain relation of the clay determined by triaxial tests
and the corresponding relations at the different model tests
corrected for the influence of the rate of strain

The stress-strain relation also varies with the density of the clay in
the sense that an increase in density will increase the shear strength
in the same way as an increase in strain rate will increase the shear
strength. This means that one stress-strain relation is valid for a
number of strain rate/density combinations.

The third presumption is fulfilled according to the investigations on
Na-smectite [2].

The copper was investigated by tensile tests. An example of such a test
is shown in Fig 4:6. Also the copper has a non-linear elasto-plastic
behaviour, the plastic state being reached at the deviatoric stress 50
MPa and 0.3% strain. The plastic behaviour is associated with strong
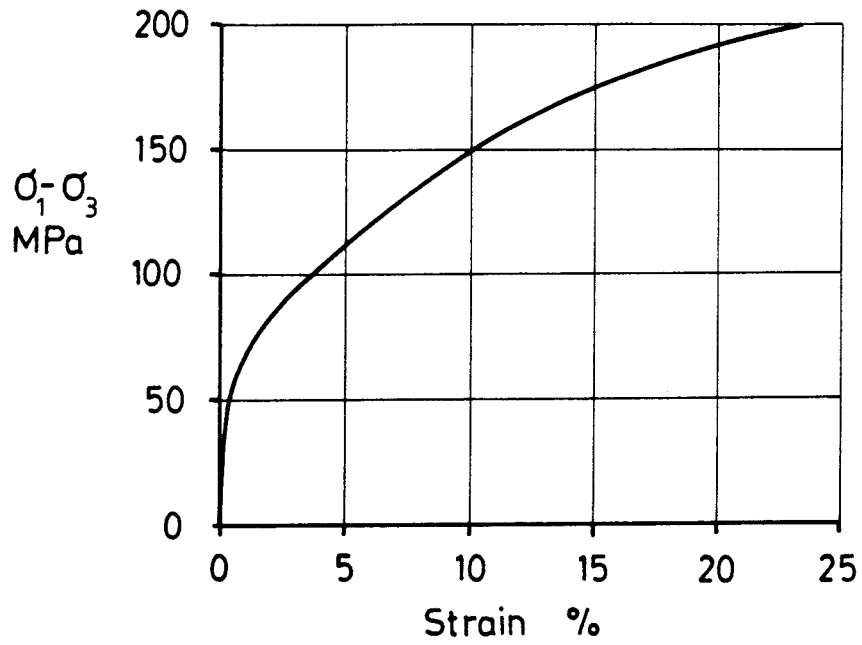strain-hardening which proceeds even after 25% strain.

17

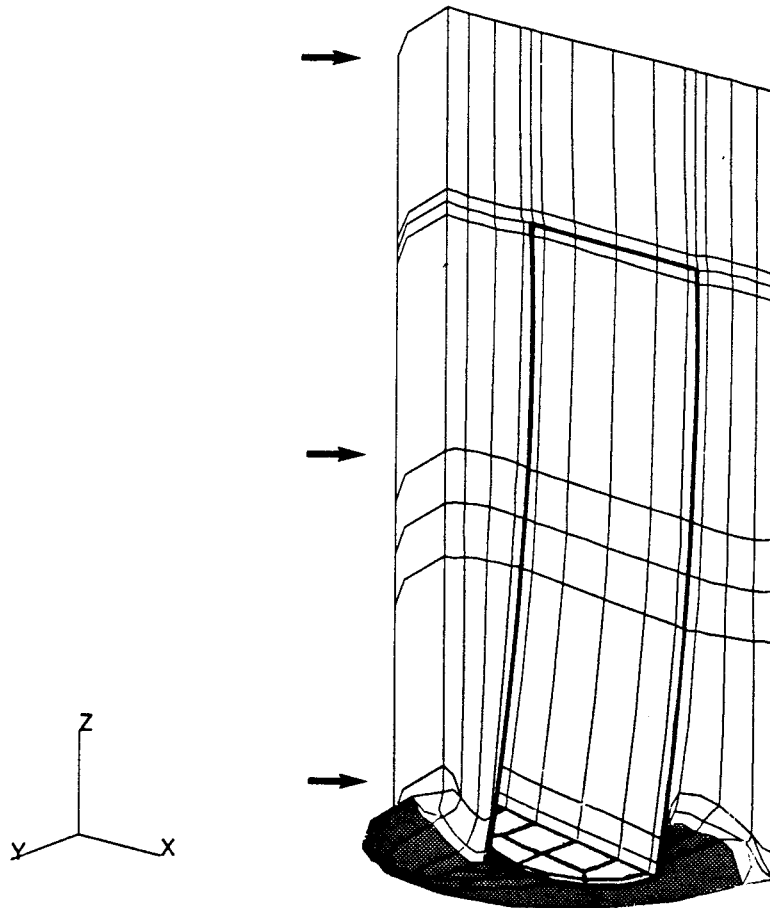Fig 4:6 Stress-strain relation of the copper used in the tests

Fig 4:7 The calculated deformed structure. The canister is marked with thick lines. The deformations are enlarged 3 times

The mathematical modelling of the stress/strain behaviour of these two materials is thus taken to be characterized by an initial linear elastic followed by a non-linear plastic stress-strain relation.

4.5 Calculation of the large scale laboratory tests

In the final calculation of the large scale test the iterations were stopped at 12 mm total shear displacement. The deformed structure after 10 mm is shown in Fig 4:7. The figure shows that the canister is deformed and the clay axially displaced, especially close to the shear plane. Plots of the deviatoric stresses and the plastic strains in the clay and the canister show that almost all the clay has yielded at 10 mm deformation with a strain as high as 200% at the shear plane. At that stage most of the the canister has started to plasticize as well.

The total force required for such a large deformation is of great interest since it is easy to measure and thus offers a nice check of the calculation. Fig 4:8 shows the calculated force as a function of the deformation together with the measured force at the three model tests. These results are analysed in the subsequent text.

4.6 Evaluation

Three main model tests were made using different rates of shear strain. The total shear was 20-30 mm and the rate of shear was 0.031 mm/s in Test 1, 1.9 mm/s in Test 2 and 160 mm/s in Test 3. The rate of strain of the clay in the model test is different at different parts of the clay embeddment since the total strain is several hundred % at the shear plane but less than one % in the top corners. The calculation which was based on a fast triaxial test, turns out to be comparable with the slow Test 1.

Fig 4:8 shows that the calculated force/deformation curve agrees very well with the experimental data. The calculated force is $\approx$ 15% higher than the force recorded in the slow test, but this deviation can be explained by a slight overestimation of the shear strength, since the actual density was 2.04 t/m^3 instead of 2.06 t/m^3.
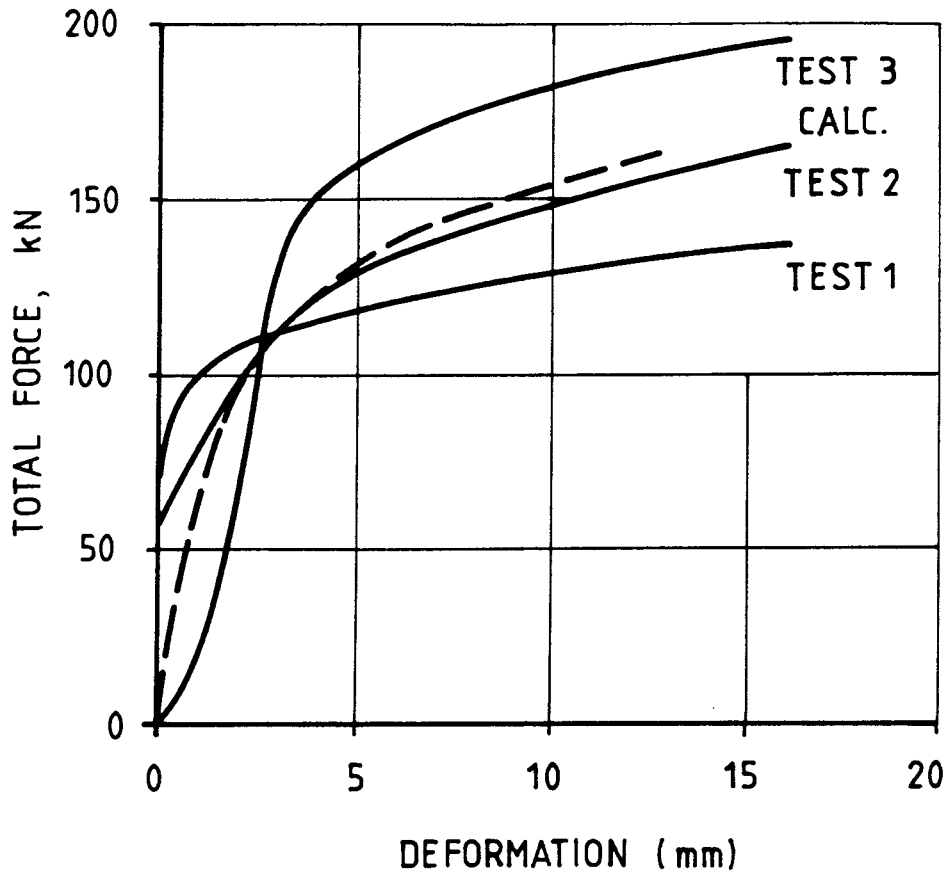
Fig 4:8 The calculated total force as a function of the shear
deformation. The results from the three model tests are also
shown

The influence of the strain rate is clearly seen in Fig 4:8, where the
increased shear resistance due to an increased shear rate is in good
agreement with $n = 0.05$ in Eqn 1.

The deformed structures studied at the excavations after the tests
resembled very much the calculated structure shown in Fig 4:7. The total
bending of the canister as well as the axial displacements of the clay
were of the same magnitude as the calculated ones.

The total pressure in the clay in the shear direction was measured both
on the canister and on the simulated rock. It was positive (compression)
$\approx$ 10 MPa after 10-15 mm shear as signalled by the four gauges closest to
the shear plane, while it was negative at the two upper gages (Nr 7 and
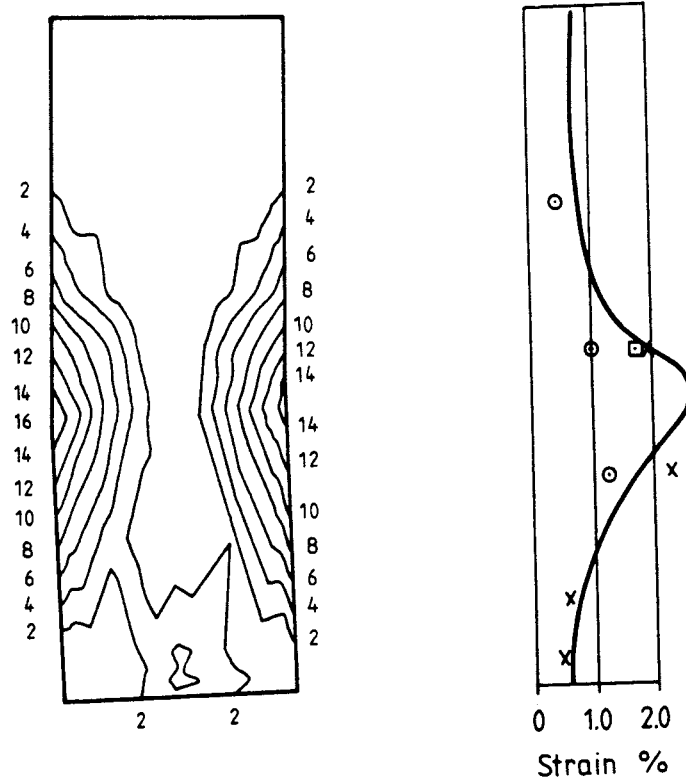10). Again, the measured stresses agreed well with the calculated ones.

Fig 4:9 The calculated plastic strain in the canister symmetri plane after 12 mm shear deformation (left) and the calculated total strain of the canister surface compared to the measured strain at the three model model tests

- Calculated
o Test 1
□ Test 2
x Test 3

The strain in the canister was measured by strain gauges glued to the canister surface in the axial direction. Fig 4:9 shows the measured strain at the different measuring points after 12 mm shear at the three different tests. The calculated strain is included in the figure and it can be seen that the agreement is good, especially at Test 3. Figure 4:9 also shows the plastic strains in the symmetry plane. The total strain, which is compared to the measured one, is obtained by adding the plastic strain to the elastic strain.

Fig 4:10 shows a picture of the deformed canister at excavation after removal of the upper "shear box" half.
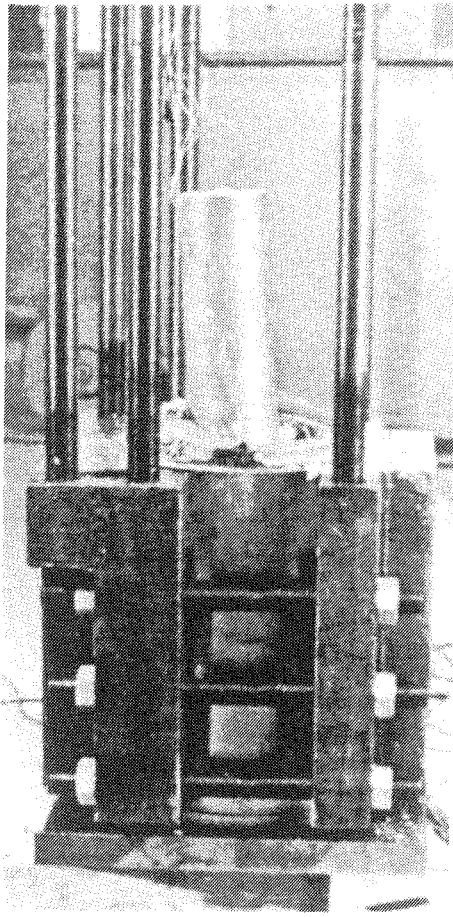
21

Fig 4:10 The deformed canister at excavation

The nice agreement between the measured and the calculated values show
that three dimensional non-linear elastic-plastic ABAQUS finite element
calculations can be used to study the effect of rock displacements on
clay embedded waste canisters. The influence of the rate of shear is
important and the optimum clay composition and density as well as
geometry can be chosen from sensitivity studies.

4.7 Sensitivity study

As shown in chapter 4.6 the comparison between the calculated and
measured results proved that the element and material models were
correct. It is thus possible to simulate other materials and other
geometries. The results from such a sensitivity study, where the density
of the clay and the thickness of the clay envelope around the canister
are changed, will be accounted for. One calculation using a hollow steel
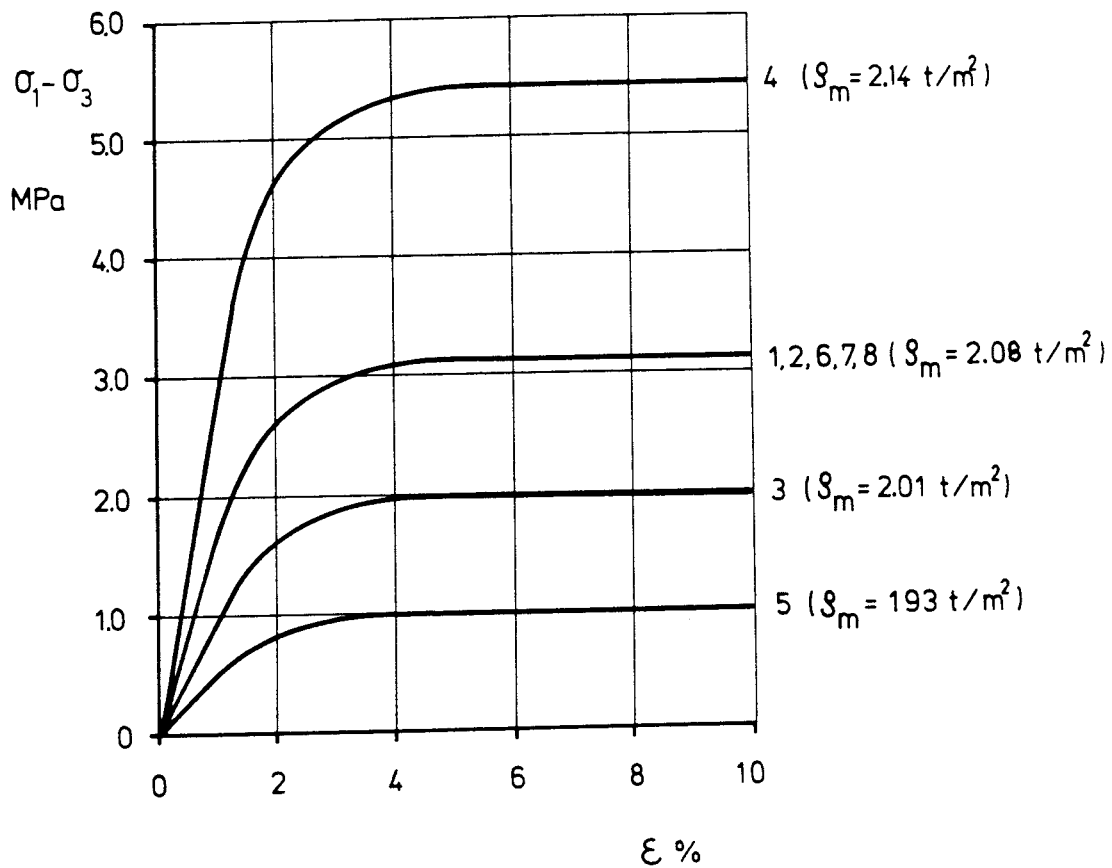canister will be shown as well.

22

Fig 4:11 Clay material models at the different calculations

Material models

Four different clay densities varying from $\rho_m = 1.93$ t/m^3 to $\rho_m = 2.14$ t/m^3 where used. The material models at these densities are shown in Fig 4:11. Most calculations where conducted simulating the density $\rho_m = 2.08$ t/m^3. The material models are related to the strain-rate corresponding to slow triaxial tests (0.6 %/h.) meaning that one complete shear would take about 12 hours. This is quite a slow shear, but a change in shear rate of a factor 10 corresponds roughly to a change in density ρ_m of 0.01 t/m^3. This means that, for a quick shear completed in a few seconds, the stress-strain relation, referred to the density $\rho_m = 2.08$ t/m^3 in the calculations, would correspond to a density of $\rho_m \approx 2.04$ t/m^3.
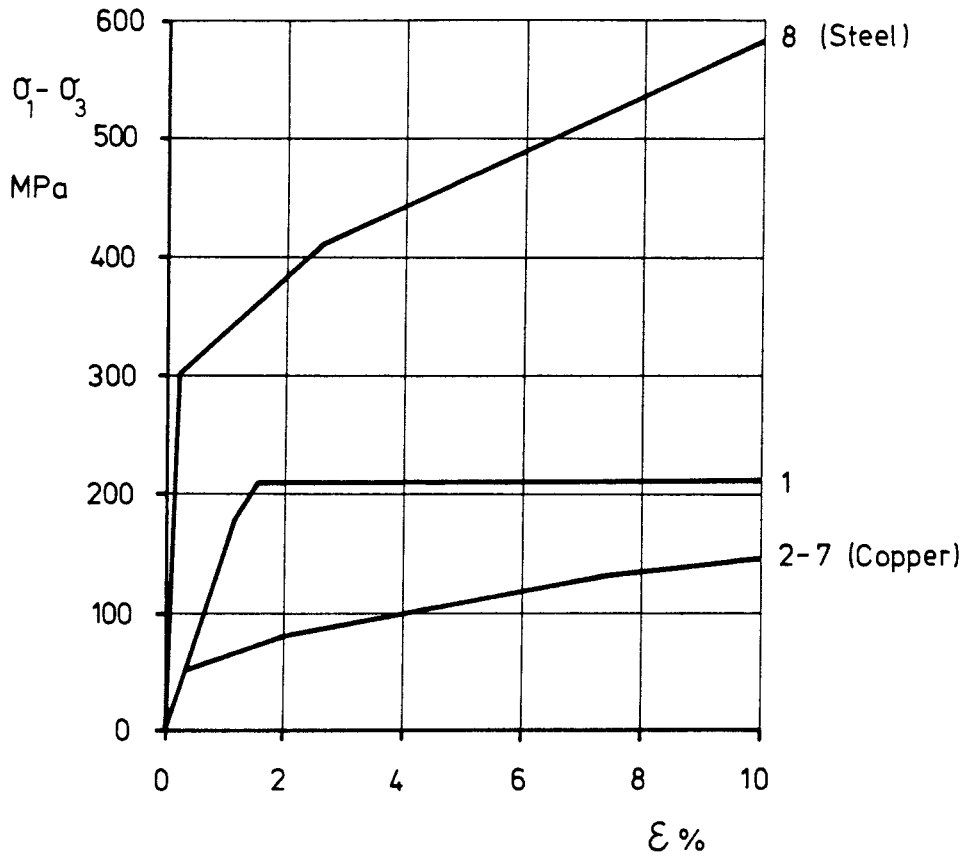
23

Fig 4:12 Canister material model at the different calculations

The material models used for the canister are shown in Fig 4:12.
Ordinary stress-strain relations for copper and steel were used in all
calculations except the first one in which a fictive model was used.

ABAQUS is usually using Mises stresses σ_j in three dimensions. In the
laboratory tests $\sigma_2 = \sigma_3$ which means that $\sigma_j = (\sigma_1 - \sigma_3)$. In the text
$(\sigma_1 - \sigma_3)$ will be called the deviatoric stress and used for describing the
material models but in the code it will be replaced by σ_j.

Calculations

8 calculations where conducted with different assumptions. The
calculations are summarized in Table I.

Table I. Summary of the sensitivity study of the rock shear

	Canister		Clay							
1	2	3	4	5	6	7	8 Max	9 Max	10	
Calc.	$(\sigma_1 - \sigma_3)_p$ MPa	$(\sigma_1 - \sigma_3)_f$ MPa	$(\sigma_1 - \sigma_3)_p$ MPa	$(\sigma_1 - \sigma_3)_f$ MPa	ρ_m t/m^3	δ cm	σ_j MPa	ε_p o/oo	% plastic	Remarks
1	50	210	1.50	3.10	2.08	1.50	120	0.90	50	fictive canister model
2	50	210	1.50	3.10	2.08	0.60	75	14.00	60	
3	50	210	0.95	1.95	2.01	1.00	60	5.00	15	
4	50	210	2.55	5.40	2.14	1.20	110	40.00	75	
5	50	210	0.47	0.97	1.93	0.87	42	0.00	0	
6	50	210	1.50	3.10	2.08	0.90	75	12.00	55	clay thickness 2.7 cm
7	50	210	1.50	3.10	2.08	0.50	75	14.00	60	clay thickness 6 cm
8	300	700	1.50	3.10	2.08	0.30	400	6.00	10	hollow steel cylinder

25

* Column 1 shows the number of the calculation

* Column 2 shows the stress when the canister starts plasticizing $(\sigma_1-\sigma_3)_y$

* Column 3 shows the failure stress of the canister $(\sigma_1-\sigma_3)_f$

* Column 4 shows the stress when the clay starts plasticizing $(\sigma_1-\sigma_3)_p$

* Column 5 shows the failure stress of the clay $(\sigma_1-\sigma_3)_f$

* Column 6 shows the simulated density at saturation ρ_m

* Column 7 shows the displacement δ at the end of the calculation
  corresponding to half the total displacement

* Column 8 shows the maximum Mises stress in the canister σ_j

* Column 9 shows the maximum plastic strain in the canister ε_p

* Column 10 shows the percentage of the canister symmetry plane that
  has started to plasticize

In calculations 1-5 the same geometry as the model tests, with a
canister diameter of 8 cm and a clay thickness of 4 cm, was used. In
calculations 6 and 7 the clay thickness was varied and calculation 8 had
the original geometry but, instead of a solid copper canister, a hollow
steel canister, with a wall thickness of 0.5 cm, was used.

Fig 4:13 shows as an example the deformed geometry in calculation 4 after
0.59 and 1.1 cm displacement, in which the density of the clay is $\rho_m =$
2.14 t/m^3. The displacements are enlarged by a magnification factor of
$F_m = 2.5$ in the figure. As can be seen, the canister is strongly deformed.
After $\delta = 1.2$ cm as much as 75% of the canister symmetry plane is
plasticized with a maximum plastic strain of 4% .

The strong influence of the density of the clay is illustrated by
comparing calculations 4 and 5 with the densities 2.14 and 1.93 t/m^3. Fig
4:14 shows Mises stresses in the symmetry plane in the upper half of the
canister after 2.9 and 9.0 mm displacement when $\rho_m = 2.14$ t/m,^{3} while Fig
4:15 shows Mises stresses after 3.0 and 8.7 mm displacement when $\rho_m = 1.93$
t/m^3. The limits for plasticizing and the limits for 1% and 2% plastic
strain are also marked in the figures. As can be seen, the canister
embedded in the dense clay is strongly plasticizing already at 3 mm
displacement, while no plasticizing has occurred, even in the most
strained part on the surface in the middle of the half-canister, when the
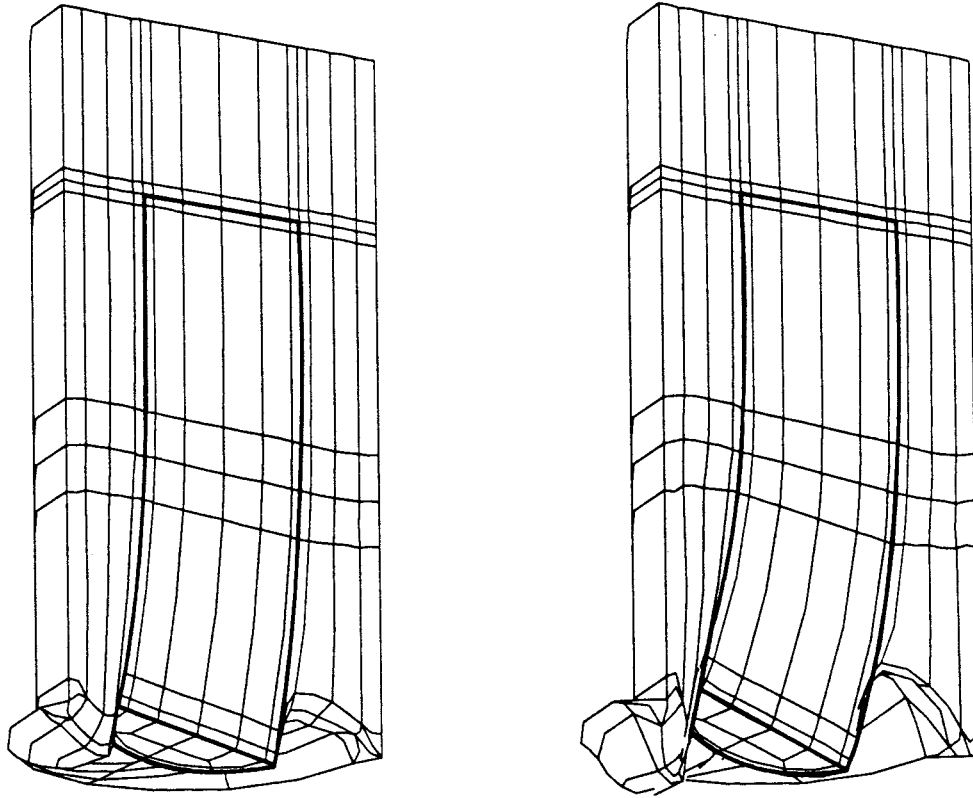density of the clay is 1.93 t/m^3.

Fig 4:13 The deformed structure after δ = 0.59 cm (left) and δ =1.1 cm. The density is ρ_m= 2.14 t/m^3 and the shear completet after $\approx$ 12 hours (very slow). The magnification factor of the displacements in the figure is 2.5. (F_m= 2.5)

The effect is very clearly seen in Fig 4:16 where the deformed canisters, surrounded by the clay with the two different densities after 8 mm displacement, are shown.

Another interesting thing that can be seen in Fig 4:15 is that the stresses in the canister have increased only by 10 - 15% when the shear displacement has increased by 200% from 3 to 9 mm. The canister is obviously only tilting in the clay when the shear strength of the clay is sufficiently low. After some displacement the whole clay surrounding the canister is yielding with a constant shear resistance, and if that shear resistance is not high enough to affect the canister, the canister will only tilt and not bend.
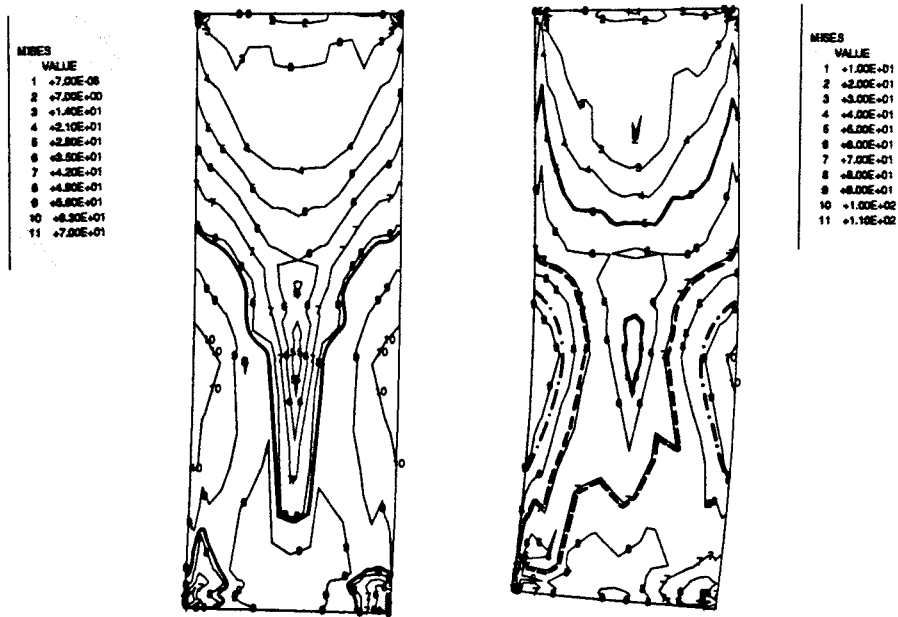
27

Fig 4:14 Mises stresses (MPa) in the canister after 2.9 mm displacement
(left) and 9.0 mm displacement at the clay density ρ_m = 2.14
t/m^3. The corresponding plastic strains are marked:

——— 0 % plastic strain

- - - - - 1 % plastic strain

—·—·— 2 % plastic strain

The influence of a changed thickness of the clay layer is illustrated in
Fig 4:17. The shear displacements are 5 mm for the clay thickness 2.7 cm
and 6 mm for the clay thickness 6.0 cm. A comparison of the maximum Mises
stress, the maximum plastic strain and the percentage of canister at yield
between the three clay thicknesses 2.7, 4.0 and 6.0 cm shows no
significant difference (columns 8 - 10 at calculations 2, 6 and 7). About
50% of the canister has started to plasticize in all three cases and the
maximum Mises stress is about 75 MPa which shows that the thickness of the
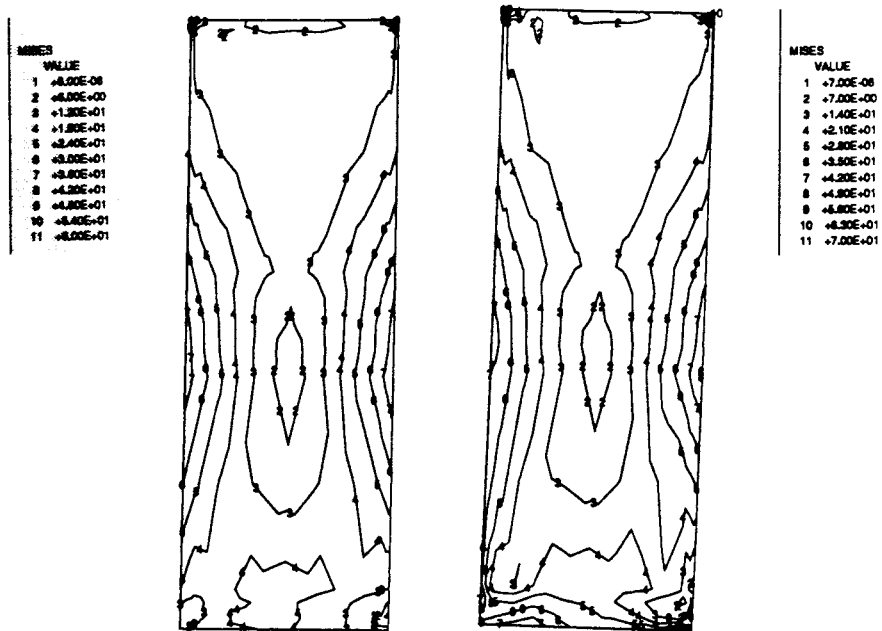clay barrier has no significant influence on the stresses and deformation
of the canister.

28

Fig 4:15 Mises stresses (MPa) in the canister after 3.0 mm displacement (left) and after 8.7 mm displacement at the clay density $\rho_m =$ 1.93 t/m^3. No plastic strains occured
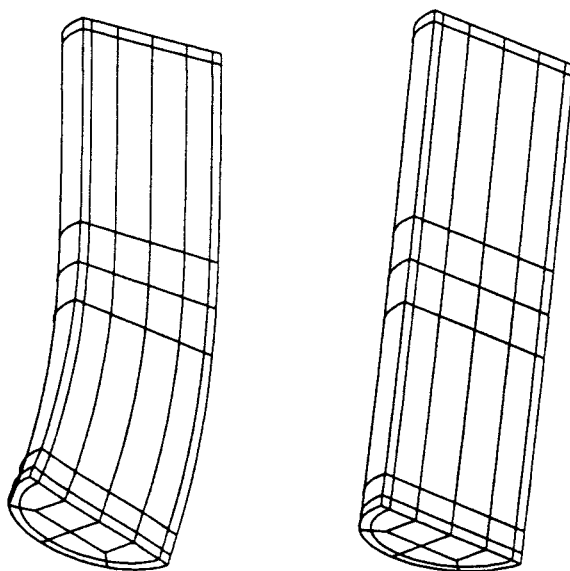

Fig 4:16 The deformed canisters after 9 mm displacement at the clay densities $\rho_m =$ 2.14 t/m^3 (left) and $\rho_m =$ 1.93 t/m^3 ($F_m \approx$ 2.5)
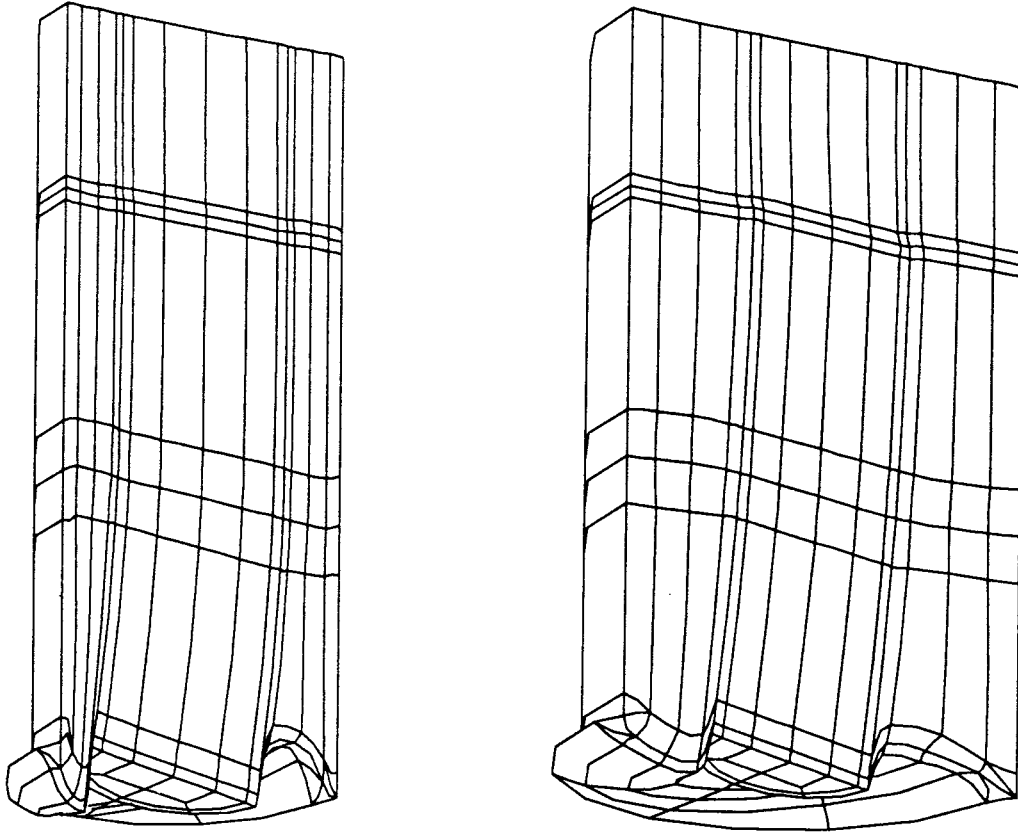
Fig 4:17 Rock shear of canisters embedded in clay with different
thickness. (F_m=2.5).
Left: Clay thickness 2.7 cm, displacement 5 mm
Right: Clay thickness 6.0 cm, displacement 6 mm

This rather surprising discovery is probably caused by the fact that a
large amount of the clay reaches its maximum shear resistance at quite a
small shear displacement and the canister is thus "floating" in the clay.
This clay thickness independence is not valid at high densities or when
buffer materials with high shear resistance are used.

Fig 4:18 shows as an example 4 plots of the stresses after 12 mm
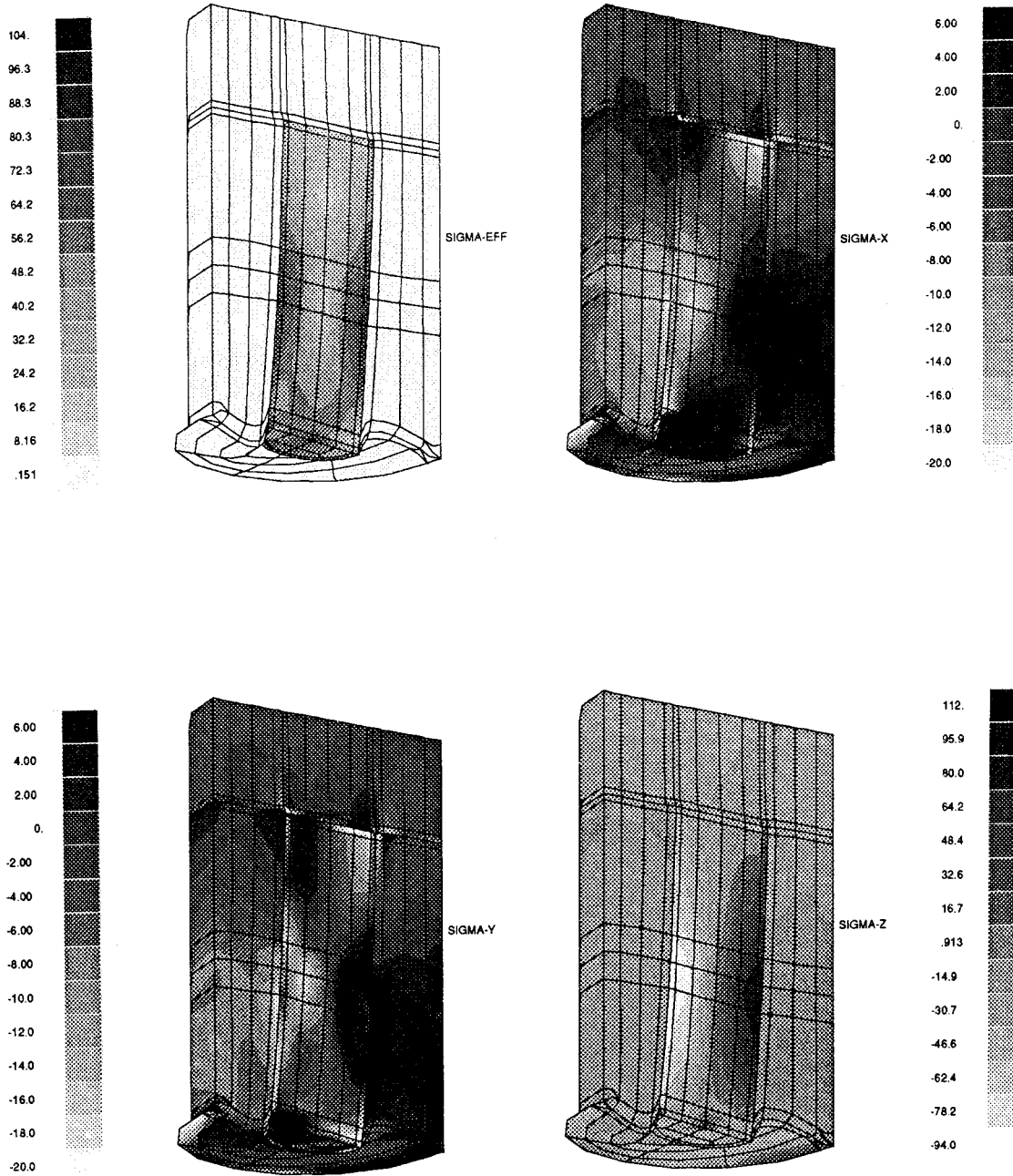displacement in calculation 7.

Fig 4:18 Mises stresses (sigma-eff) and the stresses in x, y and z direction after 12 mm displacement in calculation 7. The stresses are in MPa and negative stresses means compression in theses figures

The last calculation was made on a hollow steel cylinder with the same
geometry and clay thickness as in calculations 1 - 5. The deformed
canister is shown in Fig 4:18. The canister is somewhat less affected than
the solid copper canister due to the much higher stiffness of steel. One
interesting difference is that in the hollow canister the highest Mises
stresses occur in the shear plane and the only plasticizing takes place
close to the shear plane in contrary to the solid canister where the
plasticizing takes place in the middle of the half-canister.

4.8 Conclusions

The following main conclusions can be drawn partly from the comparisons
between the large scale laboratory tests and the calculations, and partly
from the sensitivity studies:

1) The material models and the element model are accurate and the rock
   shear calculations using the code ABAQUS are reliable

2) Only elastic deformations will take place in the copper canister
   during a rock shear if the density of the Na-bentonite is lower or
   equal to $\rho_m = 1.9$ t/m^3.

3) The thickness of the clay barrier surrounding the canister has a very
   small influence on the stresses and strains in the canister during
   a rock shear if the strength of the clay is sufficiently low, which
   is the case for Na- and Ca-bentonites at the densities considered.

4) In a hollow steel canister the plasticizing starts in the shear plane
   contrary to the solid copper canister where the plasticizing starts
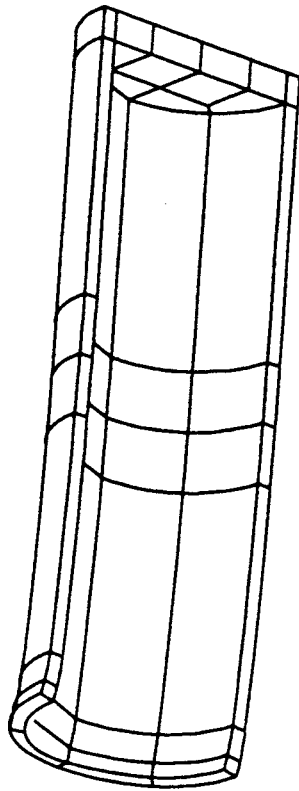   half way between the shear plane and the end face.

32

Fig 4:19 The deformed hollow steel canister after 3 mm displacement in calculation 8 (F_m=6.5)

5. CANISTER SETTLEMENT

5.1 General

While the effect of a rock shear on the canister is decreasing with decreasing density, the settlement of the canister by its own weight will increase with decreasing density. The creep settlement of the canister is modelled in order to carry out primarily the following two studies:

1) Calculate the creep settlement after a very long time.

2) Conduct sensitivity studies in order to see the effect of a change in geometry, clay density and clay composition

The modelling is not yet finished, but the present state of the work will be presented.

5.2 Material model

The creep tests in primarily triaxial cells have shown that undrained creep can be modelled according to Eqn 2 which is shown in [2] and [3].

$$\dot{\gamma} = \dot{\gamma}_0 \cdot e^{\alpha \frac{(\sigma_1 - \sigma_3)}{(\sigma_1 - \sigma_3)_f}} \cdot e^{-\alpha \frac{(\sigma_1 - \sigma_3)_0}{(\sigma_1 - \sigma_3)_f}} \cdot \left[\frac{t}{t_r}\right]^{-n} \qquad (2)$$

This relation between the creep rate $\dot{\gamma}$ and the time t after start seems to have rather constant parameters irrespective of the clay density, with the exception of the deviator stress at failure $(\sigma_1 - \sigma_3)_f$. However, Eqn 2 is only valid at medium high stress levels:

$$0.1 < (\sigma_1 - \sigma_3)/(\sigma_1 - \sigma_3)_f < 0.9$$

At low stresses, the relation is not yet determined due to measuring difficulties, but the low stress level that is achieved from the canister's own weight at high clay densities requires that knowledge.

At __medium high stresses__

$$0.1 < (\sigma_1-\sigma_3)/(\sigma_1-\sigma_3)_f < 0.9:$$

the measurements accounted for in [2] have the following parameters in Eqn 2:

The reference parameters are

$t_f = 10\ 000$ seconds

$$\frac{(\sigma_1-\sigma_3)_0}{(\sigma_1-\sigma_3)_f} = 0.5$$

The determined parameters are

$\dot{\gamma}_0 = 4.4 \cdot 10^{-8}$ 1/s

$n = 0.91$

$\alpha = 4.15$

$(\sigma_1-\sigma_3)_f$ is the failure stress which at e.g. $\rho_m = 1.96$ t/m^3 is 1.50 MPa.

At __low stresses__

$$(\sigma_1-\sigma_3)/(\sigma_1-\sigma_3)_f < 0.1$$

the following probable, but not yet determined, relation can be used:

$$\dot{\gamma} = A \left[\frac{\sigma_1 - \sigma_3}{(\sigma_1-\sigma_3)_f} \right]^a \cdot \left[\frac{t}{t_f} \right]^{-n} \tag{3}$$

with the following values of the parameters:

$A = 8.0 \cdot 10^{-8}$

$a = 1.0$

$n = 0.91$

at $t_f = 10\ 000$ seconds

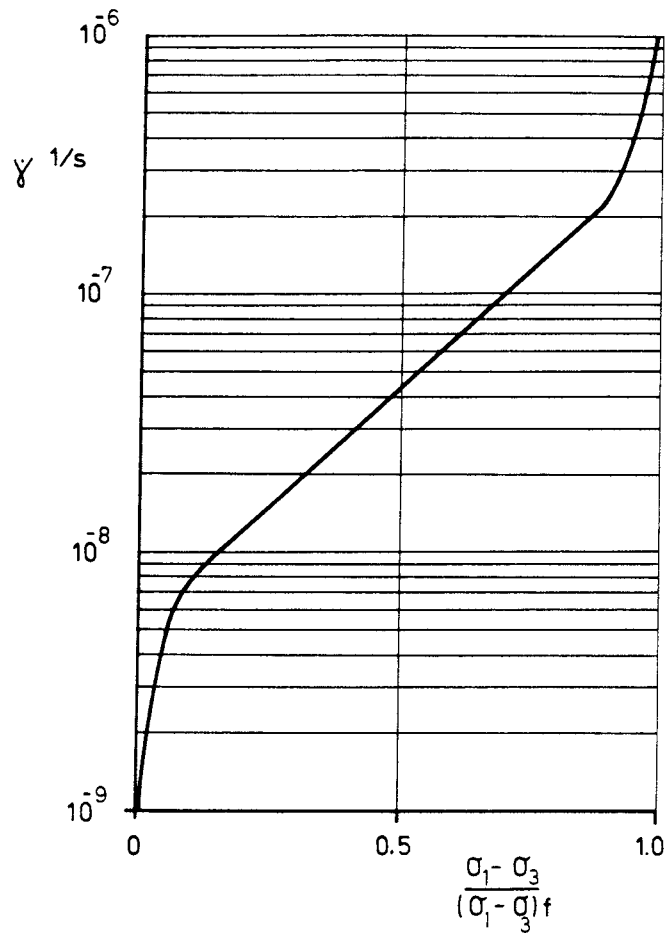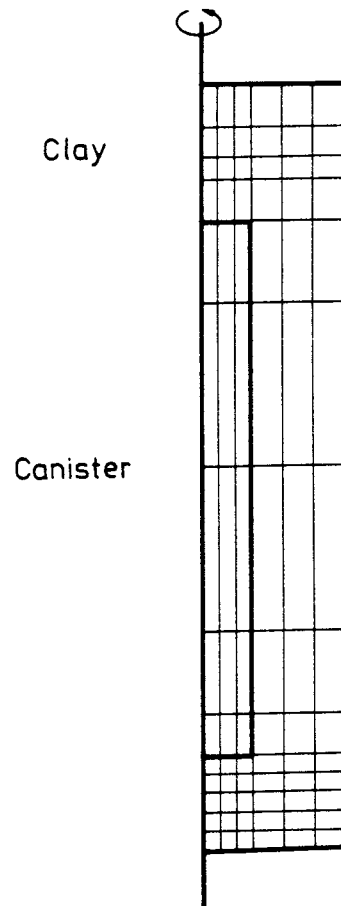Fig 5:1 Diagram of the influence of the applied deviatoric stress level $(\sigma_1-\sigma_3)/(\sigma_1-\sigma_3)_f$ on the creep rate $\dot{\gamma}$ at the reference time $t_r =$ 10 000 seconds

At **high stresses**

$$(\sigma_1 - \sigma_3)/(\sigma_1 - \sigma_3)_f > 0.9$$

the creep failure occuring after some time cannot be modelled, but the following relation can be used in the calculations:

$$\dot{\gamma} = B \left[1 - \frac{\sigma_1 - \sigma_3}{(\sigma_1 - \sigma_3)_r} \right]^{-b} \left[\frac{t}{t_r} \right]^{-n} \qquad (4)$$

with the following parameter values

36

Fig 5:2 Element model at the canister creep calculations. The model is
axi-symmetric around the left side

$B = 2.3 \cdot 10^{-8}$

$b = 1$

$n = 0.91$

at t_r 10 000 seconds

Thus the relation between the creep rate $\dot{\gamma}$ and the stress level
$(\sigma_1 - \sigma_3)/(\sigma_1 - \sigma_3)_f$ at t_f = 10 000 seconds is simulated according to Fig
5:1.

The initial settlement is pure elastic. The following E-modules can be
used:

Clay: $E = 70$ MPa (at $\rho_m = 1.96$ t/m^3)
Canister: $E = 1.6 \cdot 10^4$ MPa (copper)

5.3 Creep calculation

Two large scale tests are conducted in which the settlement can be studied. One of those tests is accounted for in [4] and the other one (a field test) is still running. The creep calculation accounted for is illustrating the calculation techniques. The element model used is shown in Fig 5:2.

The model and the effect of the own weight are symmetrical around the axis of the canister. Thus axisymmetric elements can be used and only half the model is shown in Fig 5:2.

The finite element code ABAQUS has been used at the creep calculations. The results from one calculation using fictitious parameter values are shown in fig 5:3 when the displacement in the clay and canister at different times are plotted. The displacements are enlarged 1000 times. The figure shows how the clay is moving from below the canister, along the sides, to above the canister. Since fictitious parameters have been used in this calculation, no conclusions can be drawn regarding the magnitude of the settlement.
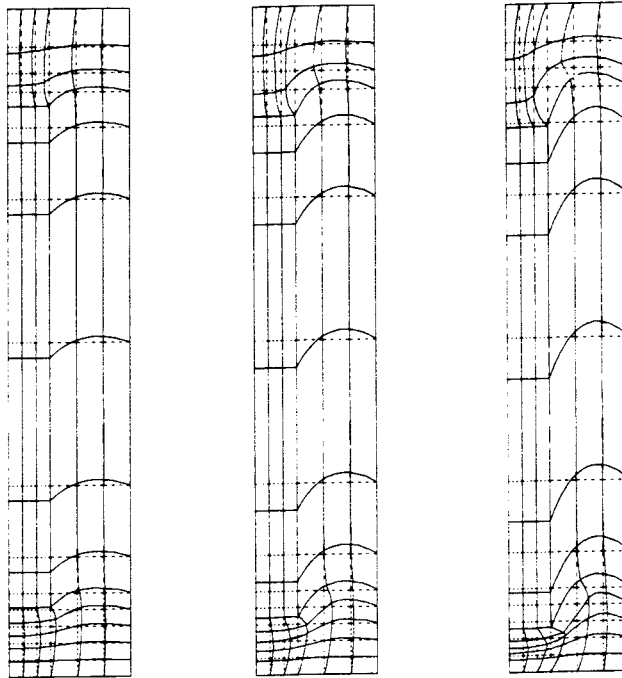
Fig 5:3 The results from the creep calculation showing (from left to right) the initial elastic response, the total displacements after 5 days and the total displacements after 2 years. $(F_m = 1000)$

——— deformed structure

----- original structure

6. THERMOMECHANICAL EFFECTS

6.1 General

A deposition hole is affected by a number of temperature pulses. The major pulse is achieved from the canister itself, while secondary pulses are coming from the neighbouring holes in the same tunnel or from other tunnels. These heat pulses are causing stresses in and volume changes of the three main components in the near field of a deposition hole: the canister, the clay and the rock.

There are two major difficulties when calculating the thermomechanical response of a heat pulse. One is the inhomogeneity of the rock which makes it improper to simulate the rock as a homogenous material. The other one is the long term creep and consolidation properties of the clay, which require a complicated material model.

These difficulties can be solved mainly by advancing stepwise. At first ordinary thermomechanical finite element calculations should be conducted, without considering the difficulties of the inhomogenous rock and the long term effects in the clay. Such a calculation will be accounted for in this chapter. The next step should be to formulate a material model that takes the consolidation and creep properties of the clay into consideration and to try to incorporate that model into the finite element calculations. The third step must be to model the fractured rock in an appropriate way.

6.2 Material models

At the first step, only the undrained response of the clay will be taken into consideration. Under those circumstances the parameters necessary for making the calculations are the elastic modulus E, the coefficient of thermal expansion α, the heat conductivity λ, the specific heat c and the density ρ. These parameters have been determined by laboratory tests.

The parameters used in the calculation are summarized in Table II:

Table II. Material parameters for the thermomechanical calculations

Material	ρ kg/m^3	λ W/m,$^\circ$K	c Ws/kg,$^\circ$K	α 1/$^\circ$K	E Pa
steel	7 700	59	460	$12 \cdot 10^{-6}$	$2.1 \cdot 10^{11}$
concrete	2 300	1.8	920	$12 \cdot 10^{-6}$	$3 \cdot 10^{10}$
sand/bentonite	2 100	2.4	1 400	$2 \cdot 10^{-4}$	$8 \cdot 10^{8}$
bentonite	2 000	1.4	1 600	$3 \cdot 10^{-4}$	$5 \cdot 10^{8}$
rock	2 700	3.6	800	$8.3 \cdot 10^{-6}$	$5 \cdot 10^{9}$

6.3 Element model

In a simulated field test a steel canister with a diameter of 20 cm and a length of 100 cm is surrounded by saturated bentonite with a density of $\rho_m = 2.00$ t/m^2. The deposition hole has a diameter of 60 cm and a length of 370 cm. The finite element model is axi-symmetric and shown in Fig 6:1, in which the deposition hole is marked with thick lines.

As shown in Table II, five materials with different properties are involved. Fig 6:2 shows the different materials in the deposition hole. Concrete is plugging the hole at the bottom and top.

The steel canister is attached to a steel tube which is free to move upwards and downwards through the compacted bentonite, the sand/bentonite mixture and the upper concrete plug. This is modelled by uncoupled double nodes in the contact area between the tube and the surrounding material.

6.4 Calculations

The calculation can be described as divided into two steps. The first step is an ordinary temperature calculation in which the temperature distribution in the element model is calculated as a function of time. The thermomechanical response to the temperature increase is calculated in the second step. These two processes are in reality coupled and performed simultaneously. The code ABAQUS is used in the calculations.
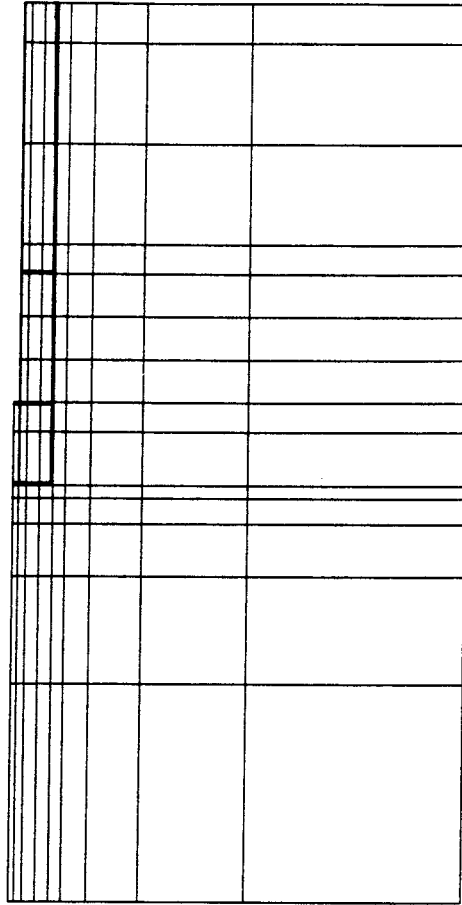
Fig 6:1 Element mesh at the thermomechanical calculation. The elements
are axi-symmetric around the left side

The power of the waste canister was simulated to be 670 W. The temperature
incease was $60^{\circ}C$ in the canister after one day, 72°C after one week and
74°C after one month. The maximum temperature increase of the rock was
$24^{\circ}C$ after one month.

The deformed structure after one week is shown in Fig 6:3, in which the
displacements are enlarged 100 times. The swelling of the saturated
bentonite, the widening of the deposition hole and the large expansion
upwards of the free steel tube are clearly seen in the figure. A slight
heaving of the rock surface (0.3 - 0.4 mm) can also be seen.

42
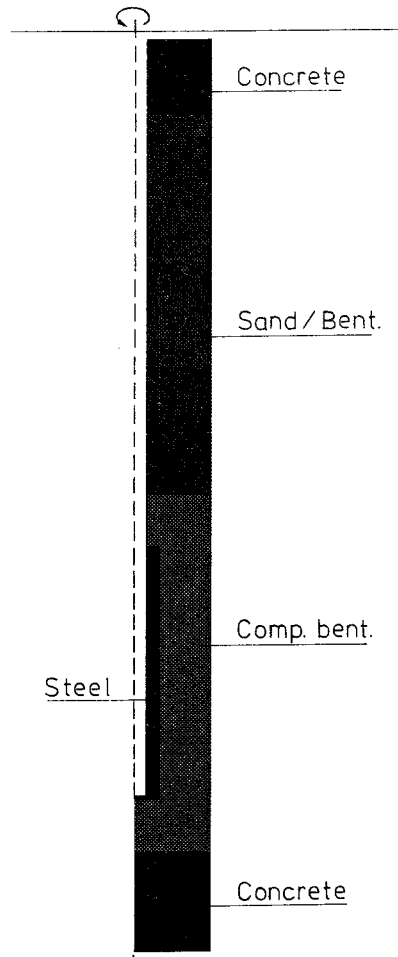
Fig 6:2 The materials with different thermomechanical properties in the
       simulated deposition hole

The calculated stresses in the canister, bentonite and rock are very high.
After 24 hours the average Mises stresses are 50 Mpa in the canister and
up to 150 Mpa in the joints. In the rock the Mises stresses are up to 30
Mpa and in the clay 60 MPa. Since the clay can only bear a few MPa Mises
stresses, it is obvious that the clay is yielding and the principal
stresses equalized.

The calculated normal stresses from the clay towards the canister and
the rock are very high (20 - 30 MPa after 24 hours) as shown in Fig 6:4.
These stresses, which are almost entirely caused by increased pore
water pressure, are calculated under the presumption of undrained
conditions. In reality the pore water will, however, probably be able to
drain through the rock fractures and the high pore pressure, which is
causing the high stresses, will dissipate with time.
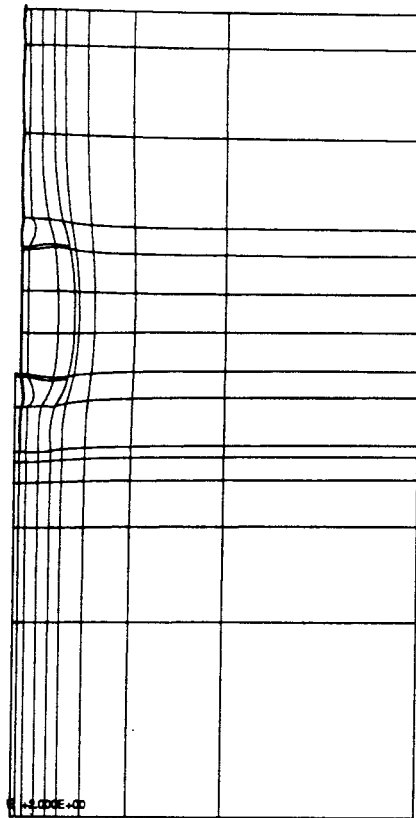
Fig 6:3 The deformed structure after one week $(F_m=100)$

The consolidation can be taken into consideration by applying the theory of consolidation by Therzaghi. The parameter required is the coefficient of consolidation c_v. Usually c_v is determined by laboratory oedometer tests using constant load. Such measurements have given the value $c_v \approx 10^{-10}$ m/s^2. The situation in a heated deposition hole is, however, not constant load but very close to constant volume, which means that the amount of pore water that must leave the clay is much less than at constant load. The time for pore pressure dissipation is thus probably much shorter at constant volume than at constant load, and the coefficient of consolidation some orders of magnitude lower. This is at present being investigated, but the corresponding coefficient of consolidation at constant volume, which can be written c_p (p would stand for change in pressure instead of change in volume), can preliminary be assigned the value $c_p = 2.5 \cdot 10^{-8}$ m/s^2.

44

Line nr	Stress MPa
1	-80
2	-71
3	-62
4	-53
5	-44
6	-35
7	-26
8	-17
9	-8
10	+1
11	+10
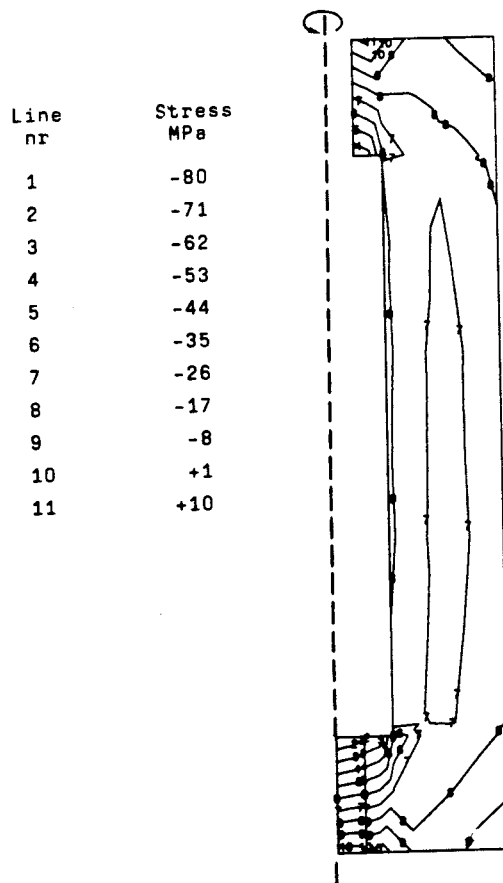
Fig 6:4 The calculated radial stresses in the bentonite (neg.=compr.)

Using c_p as described above, we find that the degree of consolidation would be $U \approx 95\%$ after already one week. The pressure towards the canister can be corrected taking the pore pressure dissipation into account, using stepwise calculations as shown in Fig 6:5. The decrease in pore pressure is calculated every second day and then added in order to give the correct pressure.

6.5 Conclusions

The calculations show that

1) the clay must be modelled as an elastic plastic material in the same way as in the rock shear scenario

2) the pore pressure dissipation regulated by c_p must be included in the clay model.
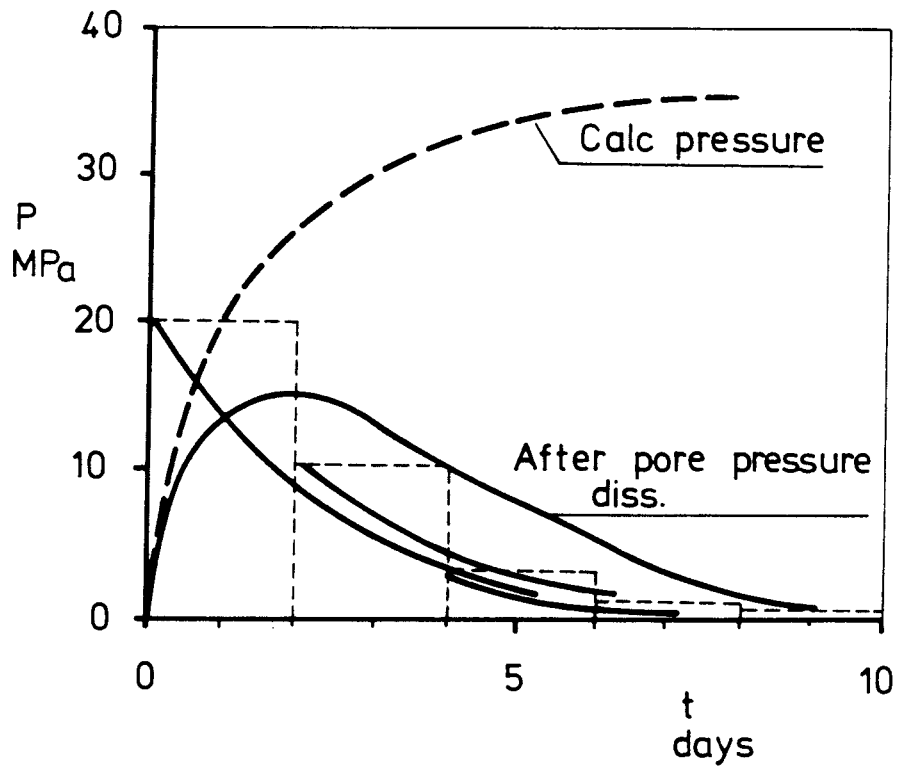
Fig 6:5 The radial pressure towards the canister from the original
calculation and after correction for pore pressure dissipation

7. SWELLING AND COMPRESSION

7.1 General

The swelling and compression of a smectite-rich clay can be divided into three sub-objects:

1) Initial undrained swelling and compression.
2) The final stage of the swelling and compression process after complete pore pressure equalization.
3) The intermediate time process mainly regulated by the drained compressibility and the hydraulic conductivity of the clay.

This chapter will deal with the total swelling or compression without considering the time process, since this problem has to be solved first.

7.2 Material model

A material model for swelling and compression must include a total knowledge of the stress-strain-strength-volume behaviour. The simple models of one-dimensional compression or compression at equal principal stresses cannot be used. The model most widely referred to, is the modified Cam-clay model which has proved to be very useful for illitic and other non-swelling clays. However, the Cam-clay model has some disadvantages when applying it to swelling clays, and an an alternative model will be used in the calculation example.

The alternative soil plasticity model that can be used is the extended Drucker-Prager theory which is usually considered appropriate for granular soils. If it is combined with porous elasticity, the large swelling and compression ability seems to be properly simulated as well. Laboratory tests and simple ABAQUS models of the laboratory tests are running simultaneously in order to confirm or modifie the theory.

7.3 Calculation example

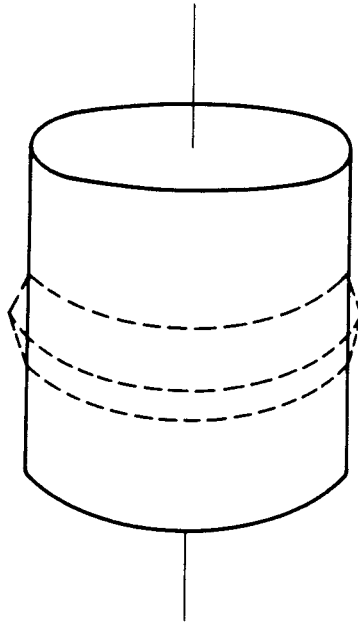The usefulness of the suggested material model will be examplified in a

Fig 7:1 The swelling of a confined axi-symmetric bentonite filling is
simulated. The dashed lines show how the confinement is widened.

scenario calculation. Fig 7:1 shows the physical model which is a confined
axi-symmetric bentonite filling. A widening of the confinement around the
material is studied. The element model and the result of the material
swelling into the widened zone is shown in Fig 7:2. The initial density
was $\rho_m = 2.08$ t/m^3 and the resulting initial swelling pressure $\sigma_s = 10.0$
MPa. Fig 7:3 shows the distribution of the average stress p after the
swelling and the volumetric strain (volume change) caused by the swelling.
The inhomogeneity of the bentonite after the swelling is obvious. The
swelling pressure ranges from almost 10.0 MPa to close to 3.0 MPa and the
maximum volumetric swelling is more than 10% corresponding to a difference
in density varying from 2.08 t/m^3 to 1.98 t/m^3. A similar evaluation of
the plastic strain shows that a large part of the clay has yielded.

48
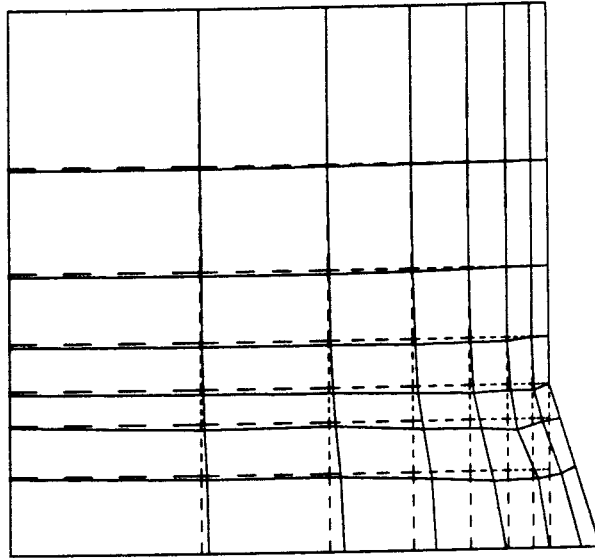
Fig 7:2 The element mesh before the swelling (dashed lines) and after the swelling (solid lines). The structure is axi-symmetric around the left boundary and the lower boundary represents a symmetry plane.

7.4 Conclusions

The calculation example using the combined Drucker-Prager and porous elasticity subroutines in ABAQUS shows the applicability of a functioning material model applied to a high standard finite element code. However, the material model must be closely studied in the laboratory tests and confirmed or modified by comparing calculated and measured scenarios.
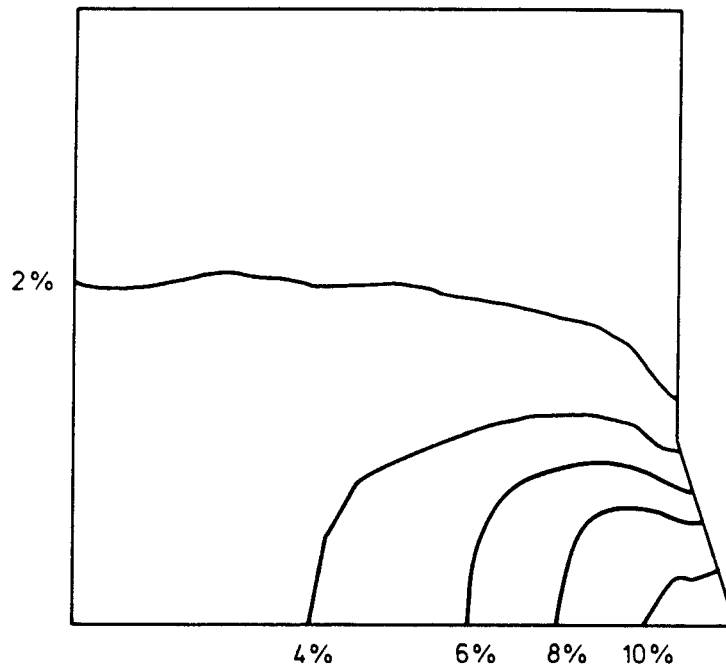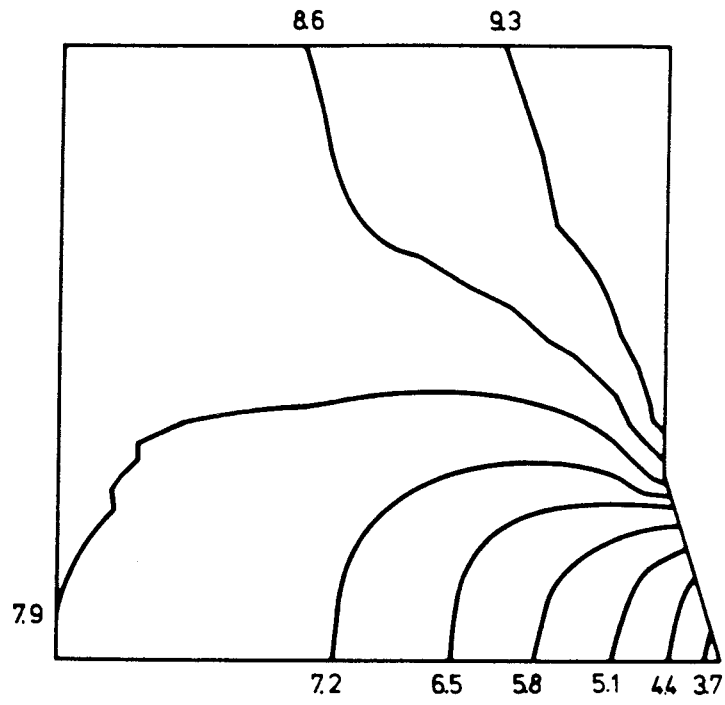
Fig 7:3 The average stress p (MPa) in the clay after swelling (above)
and the volume change ε_v caused by the swelling

50

REFERENCES

[1] Börgesson, L. 1986. Model Shear Tests of Canisters with Smectite Clay Envelopes in Deposition Holes. SKB Technical Report 86-26.

[2] Börgesson, L., Hökmark, H. and Karnland, O. 1988. Rheological Properties of Sodium Smectite Clay. SKB Technical Report 88-

[3] Börgesson, L. and Pusch, R. 1987. Rheological properties of a calcium smectite. SKB Technical Report 87-31.

[4] Pusch, R. 1986. Settlement of Canister with Smectite Clay Envelopes in Deposition Holes. SKB Technical Report 86-23.

[5] Taylor, D.W. 1948. Fundaments of Soil Mechanics. John Wiley & Sons. New York.

[6] Terzaghi, K. and Peck, R.B. 1967. Soil Mechanics in Engineering Practice, 2nd ed. John Wiley & Sons. New York.

[7] Hibbitt, Karlsson and Sorensen. ABAQUS user's manual.

List of SKB reports

Annual Reports

Technical Reports

TR 88-06
Description of geological data in SKBs database GEOTAB
Tomas Stark
Swedish Geological Co, Luleå
April 1988

TR 88-07
Tectonic studies in the Lansjärv region
Herbert Henkel
Swedish Geological Survey, Uppsala
October 1987

TR 88-08
**Diffusion in the matrix of granitic rock.
Field test in the Stripa mine. Final report.**
Lars Birgersson, Ivars Neretnieks
Royal Institute of Technology, Stockholm
April 1988

TR 88-09
The kinetics of pitting corrosion of carbon steel. Progress report to June 1987
G P Marsh, K J Taylor, Z Sooi
Materials Development Division
Harwell Laboratory
February 1988

TR 88-10
**GWHRT – A flow model for coupled groundwater and heat flow
Version 1.0**
Roger Thunvik[1], Carol Braester[2]
[1] Royal Institute of Technology, Stockholm
[2] Israel Institute of Technology, Haifa
April 1988

TR 88-11
**Groundwater numerical modelling of the Fjällveden study site – Evaluation of parameter variations
A hydrocoin study – Level 3, case 5A**
Nils-Åke Larsson[1], Anders Markström[2]
[1] Swedish Geological Company, Uppsala
[2] Kemakta Consultants Co, Stockholm
October 1987

TR 88-12
Near-distance seismological monitoring of the Lansjärv neotectonic fault region
Rutger Wahlström, Sven-Olof Linder,
Conny Holmqvist
Seismological Depertment, Uppsala University,
Uppsala
May 1988

TR 88-13
Validation of the rock mechanics HNFEMP code against Colorado school of mines block test data
Ove Stephansson, Tomas Savilahti
University of Luleå, Luleå
May 1988

TR 88-14
Validation of MUDEC against Colorado school of mines block test data
Nick Barton, Panayiotis Chryssanthakis,
Karstein Monsen
Norges Geotekniske Institutt, Oslo, Norge
April 1988

TR 88-15
**Hydrothermal effects on montmorillonite.
A preliminary study**
Roland Pusch
Ola Karnland
June 1988

TR 88-16
**Swedish Hard Rock Laboratory
First evaluation of preinvestigations 1986-87 and target area characterization**
Gunnar Gustafson
Roy Stanfors
Peter Wikberg
June 1988

TR 88-17
On the corrosion of copper in pure water
T E Eriksen[1], P Ndalamba[1], I Grenthe[2]
[1] The Royal Institute of Technology, Stockholm
  Department of nuclear chemistry
[2] The Royal Institute of Technology, Stockholm
  Department of inorganic chemistry
March 1988

TR 88-18
Geochemical modelling of the evolution of a granite-concrete-water system around a repository for spent nuclear fuel
Bertrand Fritz, Benoit Madé, Yves Tardy
Université Louis Pasteur de Strasbourg
April 1988

TR 88-19
A Bayesian nonparametric estimation of distributions and quantiles
Kurt Pörn
Studsvik AB
November 1988

TR 88-20
Creep properties of welded joints in OFHC copper for nuclear waste containment

Bo Ivarsson, Jan-Olof Österberg
Swedish Institute for Metals Research
August 1988

TR 88-21
Modelling uranium solubilities in aqueous solutions: Validation of a thermodynamic data base for the EQ3/6 geochemical codes

I Puigdomenech[1], J Bruno[2]
[1] Studsvik Nuclear, Nyköping
  Environmental Services
[2] Royal Institute of Technology, Stockholm
  Department of Inorganic Chemistry
October 1988

TR 88-22
Radiolysis of ground water: influence of carbonate and chloride on the hydrogen peroxide production

T E Eriksen[1], P Ndalamba[2], H Christensen[2],
E Bjergbakke[3]
[1] The Royal Institute of Technology, Department of
  Nuclear Chemistry, S-100 44 Stockholm, Sweden
[2] Studsvik Energiteknik AB, S-611 82 Nyköping,
  Sweden
[3] Risö National Laboratory, DK-4000 Roskilde,
  Denmark
December 1988

TR 88-23
Source parameters of major earthquakes near Kiruna, northern Sweden, deduced from synthetic seismogram computation

W T Kim, E Skordas, Y P Zohu, O Kulhanek
Seismological Department, Uppsala University,
Box 12019, S-750 12 UPPSALA
June 1988

TR 88-24
Fission product concentration profiles (Sr, Xe, Cs and Nd) at the individual grain level in power-ramped LWR fuel

R S Forsyth, O Mattsson, D Schrire
Studsvik Nuclear, Nyköping
December 1988

TR 88-25
Postglacial faulting and paleoseismicity in the Lansjärv area, northern Sweden

Robert Lagerbäck
October 1988

TR 88-26
Geological evidence of smectite longevity The Sardinian and Gotland cases

Roland Pusch, Ola Karnland
Clay Technology AB
December 1988

TR 88-27
On the formation of a moving redoc-front by a-radiolysis of compacted water saturated bentonite

Trygve E Eriksen, Pierre Ndalamba
The Royal Institute of Technology, Stockholm
Department of Nuclear Chemistry

TR 88-28
Radionuclide transport in a single fissure A laboratory flow system for transport under reducing conditions

Trygve E Eriksen
The Royal Institute of Technology, Stockholm
Department of Nuclear Chemistry
December 1988